

Superconductivity in doped Weyl semimetal $\text{Mo}_{0.9}\text{Ir}_{0.1}\text{Te}_2$ with broken inversion symmetry

Manasi Mandal,¹ Chandan Patra,¹ Anshu Kataria,¹ Suvodeep Paul,¹ Surajit Saha,¹ and R. P. Singh^{1,*}

¹*Department of Physics, Indian Institute of Science Education and Research Bhopal, Bhopal, 462066, India*

(Dated: August 24, 2021)

This work presents the emergence of superconductivity in Ir - doped Weyl semimetal T_d - MoTe_2 with broken inversion symmetry. Chiral anomaly induced planar Hall effect and anisotropic magneto-resistance confirm the topological semimetallic nature of $\text{Mo}_{1-x}\text{Ir}_x\text{Te}_2$. Observation of weak anisotropic, moderately coupled type-II superconductivity in T_d - $\text{Mo}_{1-x}\text{Ir}_x\text{Te}_2$ makes it a promising candidate for topological superconductor.

I. INTRODUCTION

Topological superconductor (TSC) is an exotic state of matter where the nontrivial topology of bulk promotes the emergence of Majorana bound states within the bulk superconducting gap [1, 2]. The realization of topological superconductors (TSCs) is a focus of research interest in condensed-matter physics due to their potential applications in fault-tolerant topological quantum computation. Theoretical studies have proposed that topological superconductivity can be induced at the interface of a topological material and a conventional superconductor [3, 4]. However, the possible complexity at the heterostructure fabrication extends the idea to search for superconductors with topological surface states. Recently, superconductivity in Weyl semimetal offers a new platform towards understanding topological superconductivity since the bulk nodal points have definite chirality and the Fermi surfaces are intrinsically topological [5]. An interesting theoretical proposal suggests that the doped Weyl semimetals with four Weyl points are natural candidates to realize higher-order topological superconductors that exhibit a fully gapped bulk state, and the surface hosts robust gapless chiral hinge states. A finite-range attractive interaction in these materials favours p+ip pairing symmetry, and such a chiral pairing state is identified as a higher-order topological superconductor [6].

MoTe_2 is a promising member of this family, having an abundant collection of structural variation with unusual attractive electronic properties, such as charge density wave (CDW) [7], an edge supercurrent [8] and surface superconductivity [9]. Noncentrosymmetric orthorhombic T_d - MoTe_2 was predicted to be type-II Weyl semimetal (WSM), which was further confirmed by experimental calculations like angle-resolved photoemission spectroscopy (ARPES) and scanning tunneling microscopy (STM) [10–13]. T_d -phase MoTe_2 shows superconductivity at transition temperature $T_C = 0.10$ K and superconducting transition temperature is sensitive to the chemical pressure [14–16]. It is worthy to mention that S-doped MoTe_2 shows two band superconductiv-

ity with $s\pm$ pairing, and the quasi-particle interference patterns with band-structure calculations reveal the existence of Fermi arcs [17, 18]. Scanning tunnelling spectroscopy (STS) studies on the surface of doped MoTe_2 reveal a much larger superconducting gap that could be interpreted as topological nontrivial superconductivity based on the pairing of Fermi arc surface states [17]. Re doping in Mo-site in MoTe_2 enhances T_C up to 4.1 K with new unconventional electronic properties like CDW, and strain-induced pseudo magnetic field and anomalous phonon behaviour [11, 19–21]. Also, the broken inversion symmetry in T_d phase MoTe_2 can generate anti-symmetric spin-orbit coupling and lift the spin degeneracy. This allows an admixture of spin-singlet and spin-triplet superconducting ground states, which may lead to host exotic time-reversal symmetry breaking ground state [22–28]. Therefore, it is essential to study superconductivity in MoTe_2 through chemical doping to identify the exotic topological states and determine the role of non-trivial topological surface states in the superconducting pairing mechanism.

In this paper, we report the emergence of superconductivity in T_d - $\text{Mo}_{1-x}\text{Ir}_x\text{Te}_2$ single crystal. It is characterised by Powder X-ray diffraction (XRD), energy-dispersive X-ray (EDAX) and temperature dependent Raman measurements to confirm the phase purity and structural phase transition. Magnetization, AC transport, specific heat measurements were performed to probe superconductivity in Ir-doped MoTe_2 system. It is observed that Ir-substitution in Mo-site enhances the superconducting transition temperature up to 2.65(3) K. Planar Hall effect and anisotropic magneto-resistance confirm the Weyl semimetallic nature after the doping. Realisation of superconductivity with intact topological surface state suggests that $\text{Mo}_{1-x}\text{Ir}_x\text{Te}_2$ as a new candidate of topological superconductor.

II. EXPERIMENTAL DETAILS

Pure phase polycrystalline samples of composition $\text{Mo}_{1-x}\text{Ir}_x\text{Te}_2$ ($x = 0$ and 0.1) were prepared from stoichiometric mixtures of Mo (99.9 % pure), Ir (99.99 % pure) and Te (99.99% pure) by the standard solid-state reaction process [19]. We tried to dope Ir with

* rpsingh@iiserb.ac.in

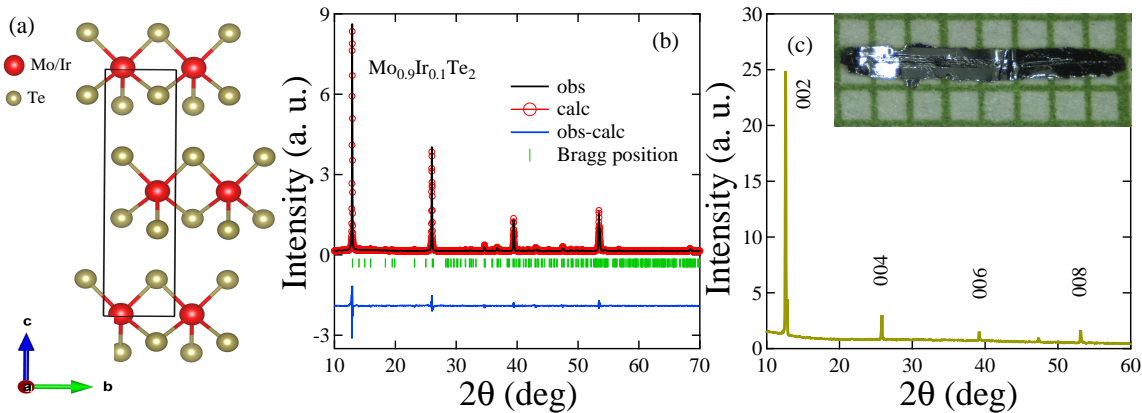


FIG. 1. (a) Room-temperature crystal structure of the $\text{Mo}_{0.9}\text{Ir}_{0.1}\text{Te}_2$ material (space group $P21/m$). (b) Rietveld refinement of powder XRD pattern for $\text{Mo}_{1-x}\text{Ir}_x\text{Te}_2$ ($x = 0.1$) recorded at room temperature. (c) Room temperature single crystal XRD shows the orientation of crystal growth along (00n) direction whereas inset shows the crystal image.

a higher percentage, but 10% was the highest possible concentration successfully achieved. Single crystals of $\text{Mo}_{1-x}\text{Ir}_x\text{Te}_2$ ($x = 0.1$) were grown by horizontal flux method with excess Te as flux [31]. Stoichiometric mixtures of Mo, Ir, and Te powders were sealed together in an evacuated quartz tube with charge and flux ratio 1:18. Crystallization was carried out at 1100°C for seven days in a box furnace, followed by the furnace switched off to avoid the hexagonal phase formation. Single crystals were trapped in the Te flux, which was taken out mechanically.

Powder x-ray diffraction (XRD) was carried out at room temperature on a PANalytical diffractometer equipped with $\text{Cu-K}\alpha$ radiation ($\lambda = 1.54056 \text{ \AA}$) for the characterization of crystal structure and phase purity. Rietveld refinement was performed using Full Prof Suite Software. Sample compositions were checked by a scanning electron microscope (SEM) equipped with an energy-dispersive X-ray (EDAX) spectrometer, which confirms Mo, Ir, and Te in the samples. The Raman spectra were measured in a Horiba JY LabRam HR Evolution Raman spectrometer and temperature-dependent Raman measurements were performed using a Linkam stage. To study the superconducting state, we measured DC and AC susceptibility by Superconducting Quantum Interference Device (SQUID MPMS, Quantum Design) at different fields. Specific heat measurements were performed by the two tau time-relaxation method in zero fields. Using the conventional four-probe technique with horizontal Rotator in the Physical Property Measurement System (PPMS, Quantum Design, Inc.), AC transport measurements were performed.

III. RESULTS AND DISCUSSION

a. Sample characterization

Polycrystalline sample was crushed in fine powder to perform XRD. The Rietveld refinement of XRD patterns confirms that the polycrystalline samples crystallized into single phase centrosymmetric monoclinic CdI_2 type structure having space group $P21/m$ as shown in Fig. 1 (b). XRD pattern of $\text{Mo}_{0.9}\text{Ir}_{0.1}\text{Te}_2$ single-crystal indicates the crystal orientation in (00n) direction (Fig. 1 (c)) and inset shows the crystal image. Raman spectra further confirms the phase purity (see Appendix B). EDAX analysis shows the presence of Ir in the single crystal though the quantity of Ir is (4%) lesser than the nominal one (see Appendix A).

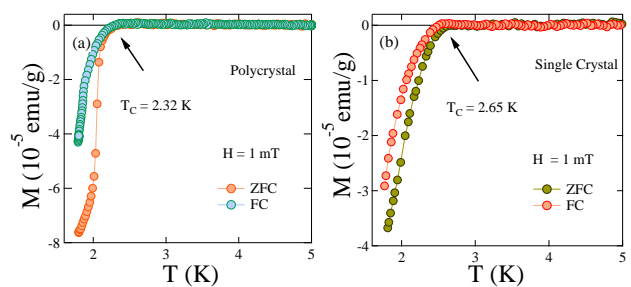


FIG. 2. (a) and (b) Temperature dependence of the dc magnetic moment on polycrystal and single crystal sample at $H = 1 \text{ mT}$.

b. Superconductivity

Superconductivity in $\text{Mo}_{0.9}\text{Ir}_{0.1}\text{Te}_2$ polycrystal and the single crystal was further confirmed by magnetization measurements. Due to the small size of the crystals

and less magnetic moments, a number of crystals were stacked together for magnetization measurements. The magnetic moment of the single crystal was checked in zero fields cooled (ZFC) and field cooled (FC) with 1 mT applied field. Fig. 2 exhibits a clear signature of type-II superconducting state with a diamagnetic signal. The polycrystalline sample shows superconducting transition temperature (T_C) at 2.32(2) K. In contrast, single-crystal yields T_C at 2.65(3) K.

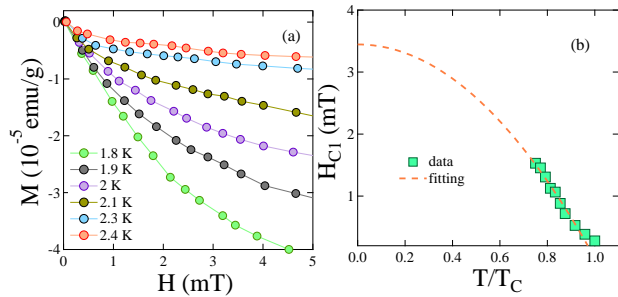


FIG. 3. (a) The low-field magnetization curves for $\text{Mo}_{0.9}\text{Ir}_{0.1}\text{Te}_2$ single crystal at different temperature. (b) Temperature dependence of the lower critical field H_{C1} was fitted using Ginzburg-Landau relation.

A sharp drop of electrical resistivity, $\rho(T)$ further confirms the superconductivity at temperature, $T_C = 2.70(2)$ K (see Appendix C). An anomaly with hysteresis in the $\rho(T)$, which is associated with the first-order structural phase transition (T_S) from $1T'$ phase to T_d phase is observed for $\text{Mo}_{0.9}\text{Ir}_{0.1}\text{Te}_2$ single crystal at 150 K, which is consistent with Raman study (see Appendix B).

To find the lower and upper critical fields, magnetic measurements were done on single crystal. We estimated the lower critical field $H_{C1}(0)$ from the low field magnetization curves $M(H)$ in the range of 0-5 mT took at different temperatures, as shown in (Fig. 3). The lower critical field, $H_{C1}(T)$, is determined from the first deviation from the linearity of the initial slope as the field is increased. $H_{C1}(0)$ was estimated to be 3.45(4) mT by fitting the data in accordance with Ginzburg-Landau (GL) equation $H_{C1}(T) = H_{C1}(0) \left(1 - \left(\frac{T}{T_C}\right)^2\right)$.

The temperature dependence of the magnetic moment under various magnetic fields was also measured to calculate the second-order transition field $H_{C2}(0)$, as shown in Fig. 4 (a). Since, in the case of a type-II material, the magnetic field can penetrate the sample and reduce the gap function, T_C shifts to lower temperature with the increment of the applied field. We estimated the value of the upper critical field by using Ginzburg-Landau (GL) formula $H_{C2}(T) = H_{C2}(0) \frac{(1-t^2)}{(1+t^2)}$, where $t = T/T_C$. The estimated value of $H_{C2}(0)$ is around 1.01(3) T as shown in Fig. 4(b).

The Ginzburg Landau coherence length $\xi_{GL}(0)$ is re-

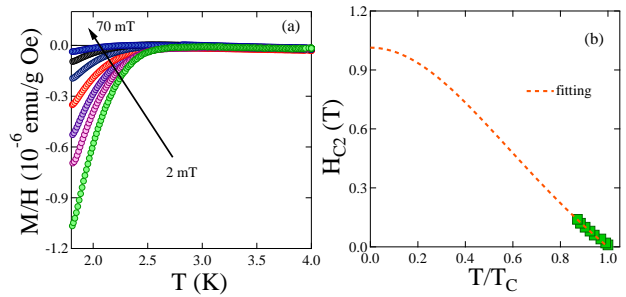


FIG. 4. (a) The $\frac{M}{H}$ curves for various applied magnetic fields. (c) $H_{C2}(0)$ was calculated by Ginzburg-Landau fits.

lated to $H_{C2}(0)$ by the relation $H_{C2}(0) = \frac{\Phi_0}{2\pi\xi_{GL}^2}$ where Φ_0 is the magnetic flux quantum having value 2.07×10^{-15} T m² [32]. The another superconducting characteristics parameter Penetration depth $\lambda_{GL}(0)$ associated with $H_{C1}(0)$ by the relation (1):

$$H_{C1}(0) = \frac{\Phi_0}{4\pi\lambda_{GL}^2(0)} \left(\ln \frac{\lambda_{GL}(0)}{\xi_{GL}(0)} + 0.497 \right) \quad (1)$$

The estimated values of $\xi_{GL}(0)$ and $\lambda_{GL}(0)$ are 180.6 Å and 2819 Å respectively. GL parameter $k_{GL} = \frac{\lambda_{GL}(0)}{\xi_{GL}(0)} = 21.2 (\gg \frac{1}{\sqrt{2}})$, indicating that $\text{Mo}_{0.9}\text{Ir}_{0.1}\text{Te}_2$ is a type-II superconductor. Thermodynamic critical field H_C is evaluated around 0.034(1) T using the relation $H_{C1}(0)H_{C2}(0) = H_C^2 \ln k_{GL}$. Breaking of Cooper pair depends on the combine consequence of Pauli paramagnetic and orbital diamagnetic effect. The Pauli limiting field within the BCS theory is given by $H_{C2}^p(0) = 1.83 T_C$, which gives $H_{C2}^p(0) = 4.85(1)$ T. In accordance to Werthamer-Helfand-Hohenberg (WHH) [33, 34] expression the upper critical field in orbital limit, $H_{C2}^{orbital}(0)$ can be calculated by the relation $H_{C2}^{orbital}(0) = -\alpha T_C \left. \frac{dH_{C2}(T)}{dT} \right|_{T=T_C}$. The obtained vale of $H_{C2}^{orbital}(0)$ is 0.67(2) T using $\alpha = 0.69$ for dirty limit superconductors and the initial slope $\left(\frac{-dH_{C2}(T)}{dT} \right) \Big|_{T=T_C} = 0.37$ calculated from $H_{C2} - T$ phase diagram. The relative strengths of the orbital and Pauli limiting values of H_{C2} is given by the Maki parameter $\alpha_M = \sqrt{2} H_{C2}^{orb}(0) / H_{C2}^p(0)$ [35]. We obtain $\alpha_M = 0.20$ indicating that orbital effect is negligible in breaking of Cooper pairs.

We have further characterized the superconducting property by angle-dependent resistivity measurements. Fig. 5(a) and (b) show the temperature dependence of resistivity for the magnetic fields $H \parallel c$ and $H \perp c$, which clearly indicates anisotropy in the upper critical field, H_{C2} . Fig. 5(c) shows the field dependence of the resistivity at different angles of H with c -axis at lowest possible temperature $T = 1.8$ K ($\simeq 0.6 T_C$). The angular dependence of $H_{C2}(\theta)$ determined from the onset value of the

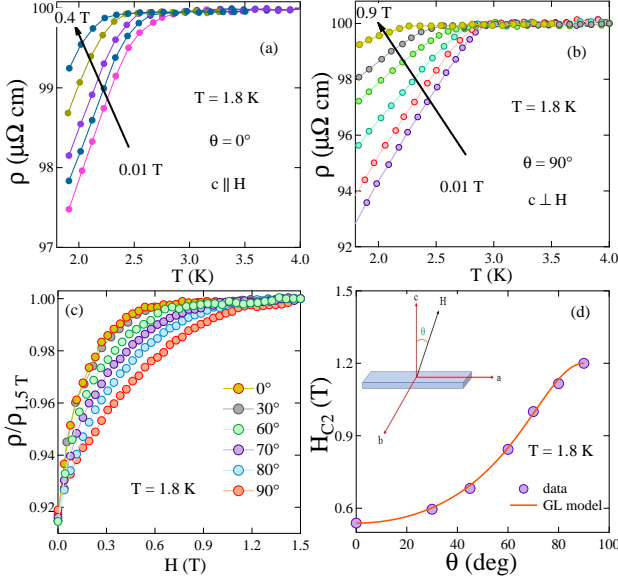


FIG. 5. Temperature dependence of electrical resistivity $\rho(T)$ at different field angle, $\theta =$ (a) 0° and (b) 90° . (c) shows field dependence of electrical resistivity $\rho(T)$ at different θ with fixed temperature, $T = 1.8$ K. (d) Angle dependent $\rho(T)$ at $T = 1.8$ K whereas solid red line is 3D GL-fit (Eq. (2)).

curve. In order to clarify the origin of the characteristic angular dependence of $H_{C2}(\theta)$, the experimental data were fitted with GL-model. According to the three dimensional (3D) anisotropic mass GL model $H_{C2}(\theta)$ can be described by the following relation [36–39]:

$$\left(\frac{H_{C2}(T, \theta)\cos\theta}{H_{C2}^\perp(T)}\right)^2 + \left(\frac{H_{C2}(T, \theta)\sin\theta}{H_{C2}^\parallel(T)}\right)^2 = 1 \quad (2)$$

The experimental data were well fitted (red solid in Fig. 5(d)) with the relation Eq. (2) with low anisotropy factor $\gamma = \frac{H_{C2}(90^\circ)}{H_{C2}(0^\circ)} = 2.1$. The nature of $H_{C2}(\theta)$ is in sharp contrast to pressure-induced two-dimensional superconductivity though the γ value is comparable [40]. Similar type of feature in $H_{C2}(\theta)$ has observed in 3D-anisotropic superconductor 2H-NbSe₂ [37–39], WTe₂ [41], and gated MoS₂ [42]. Furthermore, the in-plane, ξ_{GL}^\parallel and out-of-plane coherence lengths ξ_{GL}^\perp at $T = 1.8$ K can be extracted from the H_{C2} data, giving 247 and 166 Å. The coherence length along the c direction (ξ_{GL}^\perp) is much larger than the lattice parameter along the same direction (13.7 Å).

Heat capacity measurements were performed at zero fields, where the superconducting transition is manifested by a jump in the heat capacity data at 2.4 K (Fig. 6). The low temperature normal-state specific heat data was analyzed in the temperature range $1.9 \text{ K} \leq T \leq 8 \text{ K}$ by using the relation $\frac{C}{T} = \gamma_n + \beta_3 T^2 + \beta_5 T^4$ where, γ_n is Sommerfeld coefficient, β_3 is Debye constant and β_5 is the anharmonic contribution to the specific heat. The ex-

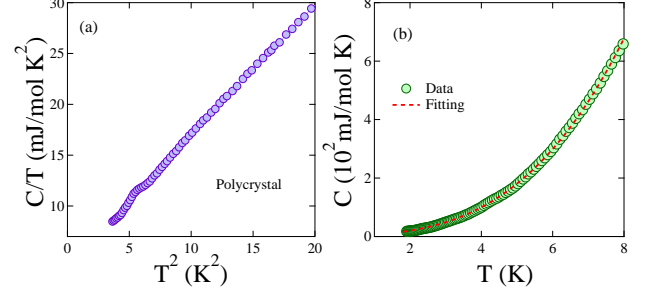


FIG. 6. (a) C/T vs T^2 at 0 Oe field. (b) shows the data fitted with $\frac{C}{T} = \gamma_n + \beta_3 T^2 + \beta_5 T^4$.

trapolation of normal state behavior below T_C , to the $T \rightarrow 0$ limits, allows the determination of normal state coefficients. The linear fits to the C/T vs T^2 gave $\gamma_n = 5.05 \pm 0.06 \text{ mJ mol}^{-1} \text{ K}^{-2}$, $\beta_3 = 1.22 \pm 0.01 \text{ mJ mol}^{-1} \text{ K}^{-4}$ and $\beta_5 = (5 \pm 0.1) \times 10^{-7} \text{ mJ mol}^{-1} \text{ K}^{-6}$ for $\text{Mo}_{0.9}\text{Ir}_{0.1}\text{Te}_2$. We calculated the Debye temperatures θ_D of the compounds using the formula $\theta_D = \left(\frac{12\pi^4 RN}{5\beta_3}\right)^{\frac{1}{3}}$ where $N (= 3)$ is the number of atoms per formula unit, R is the molar gas constant ($= 8.314 \text{ J mol}^{-1} \text{ K}^{-1}$), which was based on the simple Debye model for the phonon contribution to the specific heat. The estimated θ_D value was 168.5 K. For non-interacting fermions, the Sommerfeld coefficient, γ_n is proportional to the density of states $D_C(E_F)$ at the Fermi level which was calculated to be $2.14 \frac{\text{states}}{\text{eV f.u}}$ from the relation $\gamma_n = \left(\frac{\pi^2 k_B^2}{3}\right) D_C(E_f)$, where $k_B \simeq 1.38 \times 10^{-23} \text{ J K}^{-1}$. The strength of the attractive interaction between electron and phonon can be estimated by the electron-phonon coupling constant, λ_{e-ph} by McMillan equation [43] $\lambda_{e-ph} = \frac{1.04 + \mu^* \ln(\theta_D/1.45T_C)}{(1 - 0.62\mu^*) \ln(\theta_D/1.45T_C) - 1.04}$, where μ^* ($= 0.13$ for many superconductors) is the repulsive screened coulomb parameter. The calculated values of $\lambda_{e-ph} = 0.61$ suggesting that $\text{Mo}_{0.9}\text{Ir}_{0.1}\text{Te}_2$ is a moderately coupled superconductor such as $\text{Mo}_{1-x}\text{Re}_x\text{Te}_2$ [19], $\text{Mg}_{10}\text{Ir}_{19}\text{B}_{16}$ [44], and LaPtGe [45]. The estimated parameters for $\text{Mo}_{0.9}\text{Ir}_{0.1}\text{Te}_2$ single crystal are comparable to $\text{Mo}_{1-x}\text{Re}_x\text{Te}_2$. We have summarized all the superconducting and normal state parameters in Table I. By substituting Ir for Mo in MoTe_2 , facilitate the enhancement of the electron-phonon coupling and DOS at the Fermi energy similar to Re doped MoTe_2 compound [19]. So, we may expect unusual physical property in this system like $\text{Mo}_{1-x}\text{Re}_x\text{Te}_2$ compound. More investigation on a single crystal upto very low temperature is needed to explore the effect of Ir doping and the actual nature of the superconducting gap in this interesting system. To explore the topological nature in the Ir-doped MoTe_2 compound, we have done AC transport measurements.

TABLE I. Normal and superconducting parameters of $\text{Mo}_{0.9}\text{Ir}_{0.1}\text{Te}_2$

Parameters	Unit	$\text{Mo}_{0.9}\text{Ir}_{0.1}\text{Te}_2$	$\text{Mo}_{0.7}\text{Re}_{0.3}\text{Te}_2$ [19]
T_C^{res}	K	2.70(2)	4.1
$H_{C1}(0)$	mT	3.45(4)	5
$H_{C2}(0)$	T	1.01(3)	7.2
$H_C(0)$	T	0.034(1)	
ξ_{GL}	Å	180.6	72.2
λ_{GL}	Å	3819	
k_{GL}		21.2	
γ_n	mJ/mol K ²	5.05(6)	9
β_3	mJ/mol K ⁴	1.22(1)	
θ_D	K	165.5	
λ_{e-ph}		0.61	0.64
$D_C(E_f)$	states/eV f.u.	2.14	3.83

c. Topological Semimetallic Property

In transport experiments, WSMs usually distinctively attribute the chiral anomaly-induced negative longitudinal magnetoresistance (LMR) [46–49]. This feature indicates the nonconservation of chiral charge around the Weyl nodes due to the coplanar electric and magnetic fields ($\mathbf{E} \cdot \mathbf{B} = EB \cos \phi$) [46, 47]. The experimental observation of negative LMR is very critical in type-II Weyl semimetal due to several extrinsic effects, such as the current jetting effect. Negative LMR has not been reported in the MoTe_2 system so far within our knowledge [50, 51]. Planar Hall effect (PHE) is also a practical tool to probe the chiral charge pumping effect that directly correlates the physics of topological nature and the transport properties. Experimentally PHE is observed in T_d - MoTe_2 [52, 53] as well as other Dirac semimetals such as WTe_2 [54, 55], ZrTe_5 [56] and Cd_3As_2 [57, 58].

We have measured planar Hall resistivity on $\text{Mo}_{0.9}\text{Ir}_{0.1}\text{Te}_2$ crystal where the applied field is rotated with angle ϕ to the current direction. A schematic of planar Hall measurements is shown in the inset of Fig. 7. The obtained Hall resistivity has the total contribution of regular Hall and planar one. Normal Hall resistivity is antisymmetric under the opposite applied field, whereas the chiral-anomaly induced Hall resistivity is symmetric under the antisymmetric applied field [48, 49]. So planar hall resistivity can be extracted by average data of opposite applied field:

$$\rho_{xy}^{PHE} = [\rho_{xy}(B) + \rho_{xy}(-B)]/2 \quad (3)$$

Fig. 7 (a) shows the angular dependence of planar Hall

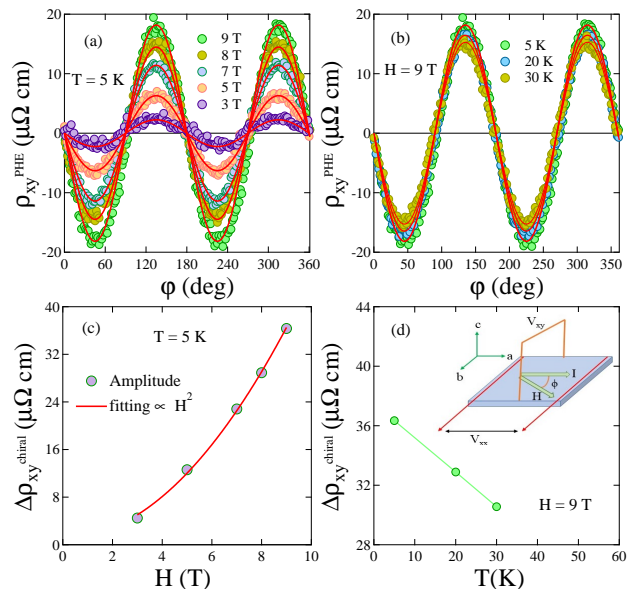


FIG. 7. The extracted intrinsic planar Hall resistivity ρ_{xy}^{PHE} (a) at $T = 5$ K under different fields (b) at $H = 9$ T under different temperatures. The variation of anisotropic resistivity, $\Delta\rho_{xy}^{PHE}$ with field and temperature is shown in (c) and (d).

resistivity at $T = 5$ K under different applied magnetic fields. Fig. 7 (b) shows the same at $H = 9$ T under different temperatures. In WSMs, chiral anomaly induced planar Hall effect (PHE) can be expressed as [48, 49]

$$\rho_{xy}^{PHE} = \Delta\rho_{xy}^{chiral} \sin\phi \cos\phi \quad (4)$$

Where $\Delta\rho_{xy}^{chiral}$ is the chiral anomaly induced anisotropic resistivity that can be expressed as $\Delta\rho_{xy}^{chiral} = \rho_{\perp} - \rho_{\parallel}$. Where ρ_{\perp} and ρ_{\parallel} are the resistivity corresponding to the magnetic field perpendicular to and along the direction of the current flow (I).

Fig. 7 shows that angular dependence of ρ_{xy}^{PHE} has a period of π with maximums appear at 45° and 135° similar to MoTe_2 and several other topological semimetals. We have fitted the data at $T = 5$ K with Eq. (4) and plotted the field dependence of $\Delta\rho_{xy}^{chiral}$ in Fig. 7(c), which follows quadratic nature as expected for chiral anomaly induced PHE. Temperature dependence of $\Delta\rho_{xy}^{chiral}$ at $H = 9$ T is also shown in Fig. 7(d) which decreases with increases temperature similar to the nature of DSMs and WSMs.

Anisotropic magnetoresistivity (AMR), $\Delta\rho_{xx}$ can also be observed by the angular dependence (ϕ) of longitudinal resistivity ρ_{xx} . In WSMs, chiral anomaly related AMR can be expressed as [48, 49]:

$$\rho_{xx} = \rho_{\perp} - \Delta\rho_{xx}^{chiral} \cos^2\phi \quad (5)$$

Fig. 8(a) shows the the angular dependence (ϕ) of ρ_{xx} at $T = 5$ K under different applied fields. The data

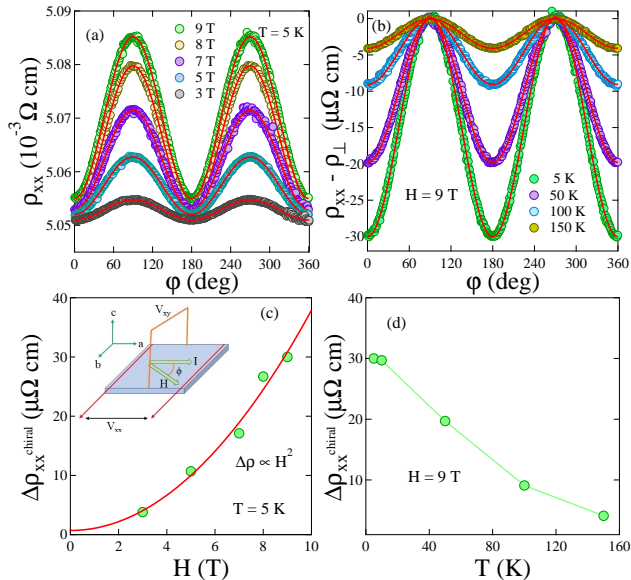


FIG. 8. (a) Angle dependent ρ_{xx} at $T = 5$ K under different fields whereas (b) shows the angle dependent $(\rho_{xx} - \rho_{\perp})$ at $H = 9$ T under different temperatures. The solid curve is a fit to equation. The variation of anisotropic resistivity, $\Delta\rho_{xx}$ with field and temperature extracted from fitting is shown in (c) and (d).

were fitted by the Eq. (5), and $\Delta\rho_{xx}^{chiral}$ was extracted for a different field. We have shown the field variation of $\Delta\rho_{xx}^{chiral}$ in Fig. 8(c) that fitted well with quadratic equation ($\Delta\rho_{xx}^{chiral} \propto H^2$). The nature of the curve is consistent to Fig. 7(c). The slight variation in value of $\Delta\rho_{xx}^{chiral}$ and $\Delta\rho_{xy}^{chiral}$ be due to the sample dimensions used for the purpose of the measurements.

Fig. 8(b) shows the temperature dependence of $\rho_{xx} - \rho_{\perp}$ taken at various temperature at constant applied magnetic field $H = 9$ T. The data were fitted with Eq. (5) which yields temperature dependence of $\Delta\rho_{xx}^{chiral}$ as shown in Fig. 8(d). Similar nature was observed in Fig. 8(d) validating our measurements and analysis.

It is observed that nontrivial Berry-curvature-induced PHE is pronounced in Ir-doped T_d - MoTe_2 and still visible upto 150 K. The quadratic field dependence of $\Delta\rho_{xx}^{chiral}$ indicates the weak chiral anomaly induced coupling strength between electric and chiral charge whereas parent MoTe_2 shows intermediate coupling strength with high field at $T \leq 50$ K [53]. The change in coupling strength may be due to the small change in lattice constant or carrier concentration due to Ir-doping similar to the theoretical prediction [59, 60].

IV. CONCLUSION

In summary, we have successfully prepared polycrystal and single crystal of $\text{Mo}_{1-x}\text{Ir}_x\text{Te}_2$ ($x = 0$ and 0.1) compound crystallized into a centrosymmetric monoclinic

structure having space group P21/m. Magnetization measurements reveal that $\text{Mo}_{0.9}\text{Ir}_{0.1}\text{Te}_2$ is a type-II superconductor with a transition temperature of $2.65(3)$ K, which is 26 times enhanced with respect to parent MoTe_2 . Resistivity measurements indicate that structural transition is decreased with Ir doping similar to the Re-doping effect in MoTe_2 compound. Raman study confirms the phase purity and $1T'$ to T_d structural phase transition at $T_S \simeq 150$ K. Angle-dependent higher critical field, $H_{C2}(\theta)$ follows 3D anisotropic GL-model with factor 2.1. The enhanced density of states, electron-phonon coupling, and other estimated values of superconducting and normal state parameters make $\text{Mo}_{0.9}\text{Ir}_{0.1}\text{Te}_2$ compound interesting to study further to explore unusual attractive electronic state like Re-doped MoTe_2 system. Above all, exotic chiral anomaly induced PHE is observed up to 150 K in $\text{Mo}_{1-x}\text{Ir}_x\text{Te}_2$ ($x = 0.1$). We can conclude this system as a possible topological superconductor with an exotic angle-dependent higher critical field. Further microscopic investigations like muon spectroscopy and scanning tunneling microscopy required to probe superconducting gap symmetry and ground state.

V. ACKNOWLEDGMENTS

R. P. S. acknowledges the Science and Engineering Research Board, Government of India for the Core Research Grant CRG/2019/001028. S. S. acknowledges the Science and Engineering Research Board, Government of India for the Research Grant ECR/2016/001376. Authors thank Mr. Devesh Negi [CSIR fellow, File No.: 09/1020(0139)/2018-EMR-I] and Ms. Bommareddy Poojitha for their help with the Raman measurements.

Appendix A: Characterization

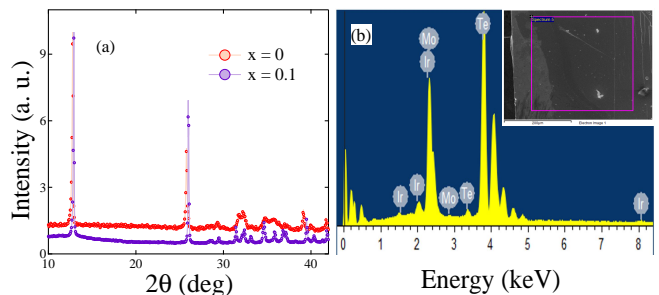


FIG. 9. (a) Room temperature powder XRD pattern for $x = 0$ and 0.1 (b) EDX pattern for $x = 0.1$.

EDAX analysis is summarized in Table II.

TABLE II. Average elemental concentration (average of 10 points) obtained from the EDS measurements for $\text{Mo}_{1-x}\text{Ir}_x\text{Te}_2$ ($x = 0.1$) samples.

	Nominal composition	From EDS
Polycrystal	$\text{Mo}_{0.9}\text{Ir}_{0.1}\text{Te}_2$	$\text{Mo}_{0.9}\text{Ir}_{0.08}\text{Te}_2$
Single crystal	$\text{Mo}_{0.9}\text{Ir}_{0.1}\text{Te}_2$	$\text{Mo}_{0.9}\text{Ir}_{0.04}\text{Te}_2$

Appendix B: Raman Study

Micro-Raman measurements are very effective in confirming the phase purity of investigated samples down to micron length scales. The micro-Raman measurements reported here were performed at a laser spot size of $0.67 \mu\text{m}$, thereby allowing the investigation of any impurity phase with a spatial resolution of $< 1 \mu\text{m}$. Fig. 10(a) compares the room-temperature Raman spectra of MoTe_2 and $\text{Mo}_{0.9}\text{Ir}_{0.1}\text{Te}_2$. The Raman modes observed in pure MoTe_2 are labelled as P_1 - P_9 , which correspond to out-of-plane vibrations with symmetries A_g or B_g [61–64]. We also observe that the room-temperature Raman spectrum obtained for $\text{Mo}_{0.9}\text{Ir}_{0.1}\text{Te}_2$ shows similar modes as in for the pure phase, thus, confirming the absence of any impure phases in the investigated flakes. In addition to the confirmation of the phase purity, our temperature-dependent Raman measurements provide evidence of the topological phase transition in $\text{Mo}_{0.9}\text{Ir}_{0.1}\text{Te}_2$ at $\approx 150 \text{ K}$ from a crystallographic point of view. Fig. 10(b) shows the Raman spectra obtained for $\text{Mo}_{0.9}\text{Ir}_{0.1}\text{Te}_2$ at various temperatures. We clearly observe a splitting of the P_6 mode into two bands (P_{6A} and P_{6B}) below $\approx 150 \text{ K}$. A similar observation of mode-splitting was previously reported for pure [11, 61–64] and Re-doped MoTe_2 [11], attributed to the topological phase transition from the high-temperature $1T'$ to low-temperature T_d phase. Importantly, the topological phase transition is associated with a structural transformation characterized by a modification of the layer stacking order. The high-temperature phase ($1T'$) has a monoclinic structure possessing a center of inversion symmetry, while the low-temperature phase (T_d) is orthorhombic without the inversion symmetry. Therefore, the topological phase transition is associated with a breaking of inversion symmetry, which is also a fundamental requirement for the appearance of the Weyl semimetallic phase, that can be probed using Raman spectroscopy. The splitting of the P_6 mode is a result of the renormalization of phonons induced by the breaking of inversion symmetry at $\approx 150 \text{ K}$. The observation also matches well with the AC transport measurements (Appendix C), which show a hysteretic change in $\rho(T)$ around $\approx 150 \text{ K}$ (Fig. 11).

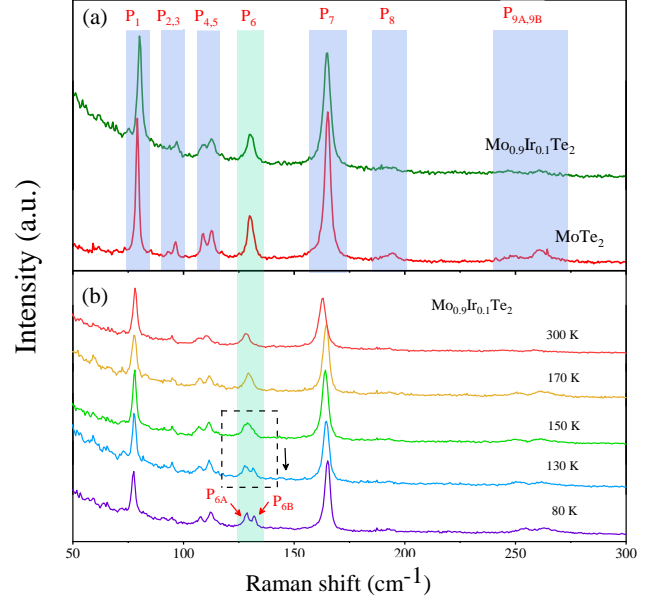


FIG. 10. (a) A comparison of the room temperature Raman spectra of MoTe_2 and $\text{Mo}_{0.9}\text{Ir}_{0.1}\text{Te}_2$. (b) Raman spectra of $\text{Mo}_{0.9}\text{Ir}_{0.1}\text{Te}_2$ taken at different temperature revealing the splitting of the P_6 mode to P_{6A} and P_{6B} at low temperature.

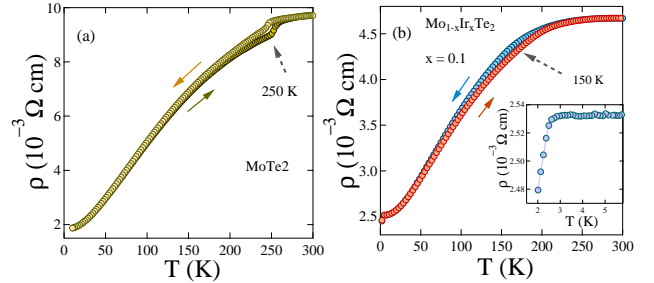


FIG. 11. Normal state resistivity data $\rho(T)$ over the temperature range $1.9 \text{ K} \leq T \leq 300 \text{ K}$. A hysteresis in $\rho(T)$ observed under the cooling and warming modes indicates polar structural transition temperature as shown by arrow symbol. Inset of (b) highlights the superconducting phase transition for $x = 0.1$.

Appendix C: AC Transport Measurements

Electrical resistivity, $\rho(T)$ were measured on $\text{Mo}_{1-x}\text{Ir}_x\text{Te}_2$ ($x = 0$ and 0.1) single crystal samples over the temperature range $1.9 \text{ K} \leq T \leq 300 \text{ K}$ in zero magnetic field in the cooling and warming modes. An anomaly with hysteresis in the $\rho(T)$, which is associated with the first-order structural phase transition (T_S) from $1T'$ phase to T_d phase is observed for both the samples ($x = 0$ and 0.1). The polar structural transition temperature, T_S , is found at around 240 K in parent MoTe_2 whereas the same has decreased to 150 K for $\text{Mo}_{0.9}\text{Ir}_{0.1}\text{Te}_2$, which is consistent with Raman study. The structural transition temperature is indicated by an arrow symbol in

Fig. 11. Similar type behaviour of resistivity was observed in Re-doped MoTe_2 system [19]. A sharp drop of $\rho(T)$ is observed in $\text{Mo}_{0.9}\text{Ir}_{0.1}\text{Te}_2$ sample at temperature, $T_C = 2.70(2)$ K. This type of nature indicates the superconducting phase transition.

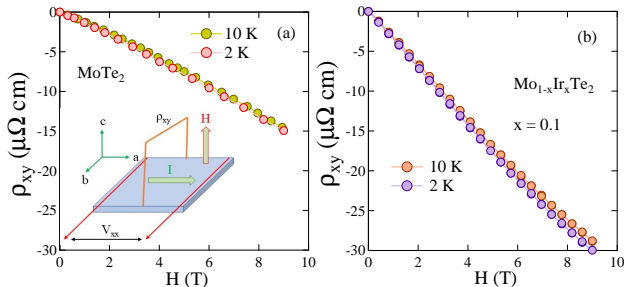


FIG. 12. Regular Hall measurements performed on $\text{Mo}_{1-x}\text{Ir}_x\text{Te}_2$ ($x = 0$ and 0.1) at 10 K and 2 K upto 9 T.

In order to find the nature of carrier we have performed regular Hall effect on the ab plane with the applied field along the c -direction (Hall configuration is shown in Fig. 12). The linear field dependence of hall resistivity shows negative slope indicating the dominating electron carrier in $\text{Mo}_{0.9}\text{Ir}_{0.1}\text{Te}_2$ system as shown in Fig. 12. Ir doping may enhance the electron concentration in the system similar to Re doping in Mo-site [19].

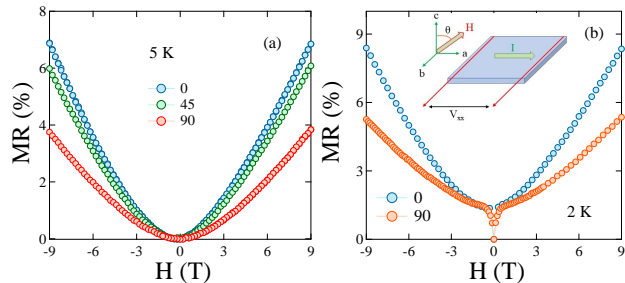


FIG. 13. MR data taken at 5 K and 2 K on $\text{Mo}_{0.9}\text{Ir}_{0.1}\text{Te}_2$ crystal at different magnetic angles, θ between the direction of c -axis and applied magnetic field.

We have also measured magneto-resistance (MR) on Ir-doped crystal at 5 K and 2 K at different angles, θ between the c -axis and magnetic field direction, H . The magnetic field dependence of the MR is defined as $\frac{\rho_{xx}(H) - \rho_{xx}(0)}{\rho_{xx}(0)}$. As shown in Fig. 13(a) and (b), MR decreases with increasing angle θ from 0° to 90° at 5 K and 2 K, suggesting an anisotropy of transport behavior. MR data at $T = 2$ K indicates the superconducting nature at low field region. MR data suggests that magneto-resistance has been suppressed with Ir-doping in MoTe_2 system which may be due to the emergence of superconductivity [53].

- [1] X. L. Qi and S. C. Zhang, Rev. Mod. Phys. 83, 1057 (2011).
- [2] C. Nayak, S. H. Simon, A. Stern, M. Freedman, and S. Das Sarma, Rev. Mod. Phys. 80, 1083 (2008).
- [3] N. Read and D. Green, Phys. Rev. B 61, 10267 (2000).
- [4] L. Fu and C. L. Kane, Phys. Rev. Lett. 100, 096407 (2008).
- [5] J. Wang, Natl. Sci. Rev. 6, 2 (2019).
- [6] A. Jahin, A. Tiwari, and Y. Wang, arXiv:2103.05010 (2021).
- [7] L. Wang, Y. Wu, Y. Yu, A. Chen, H. Li, W. Ren, S. Lu, S. Ding, H. Yang, Q.-K. Xue, F.-S. Li, and G. Wang, ACS Nano 14, 8299 (2020).
- [8] W. Wang, S. Kim, M. Liu, F. Cevallos, R. Cava, and N. Ong, Science 368, 534 (2020).
- [9] Y. Naidyuk, O. Kvitnitskaya, D. Bashlakov, S. Aswartham, I. Morozov, I. Chernyavskii, G. Fuchs, D. stefan Ludwig, R. Hühne, K. Nielsch, B. Buchner, and D. Efremov, 2D Mater. 5 (2018).
- [10] K. Deng, G. Wan, P. Deng, K. Zhang, S. Ding, E. Wang, M. Yan, H. Huang, H. Zhang, Z. Xu, J. Denlinger, A. Fedorov, H. Yang, W. Duan, H. Yao, Y. Wu, S. Fan, H. Zhang, X. Chen, and S. Zhou, Nat. Phys. 12, 1105 (2016).
- [11] S. Paul, S. Karak, M. Mandal, A. Ram, S. Marik, R. P. Singh, and S. Saha, Phys. Rev. B 102, 054103 (2020).
- [12] J. Jiang, Z. K. Liu, Y. Sun, H. F. Yang, C. R. Rajamathi, Y. P. Qi, L. X. Yang, C. Chen, H. Peng, C. C. Hwang, S. Z. Sun, S. K. Mo, I. Vobornik, J. Fujii, S. S. P. Parkin, C. Felser, B. H. Yan, and Y. L. Chen, Nat. Commun. 8, 13973 (2017).
- [13] P. Deng, Z. Xu, K. Deng, K. Zhang, Y. Wu, H. Zhang, S. Zhou, and X. Chen, Phys. Rev. B 95, 245110 (2017).
- [14] F. Chen, X. Luo, R. Xiao, W. Lu, B. Zhang, H. Yang, J. Li, Q. Pei, D.-F. Shao, R. Zhang, L. Ling, C. Xi, W. Song, and Y. Sun, Appl. Phys. Lett. 108, 162601 (2016).
- [15] H. Takahashi, T. Akiba, K. Imura, T. Shiino, K. Deguchi, N. K. Sato, H. Sakai, M. S. Bahramy, and S. Ishiwata, Phys. Rev. B 95, 100501 (2017).
- [16] P. Li, J. Cui, J. Zhou, D. Guo, Z. Zhao, J. Yi, J. Fan, Z. Ji, X. Jing, F. Qu, C. Yang, L. Lu, J. Lin, Z. Liu, and G. Liu, Adv. Mater. 31, e1904641 (2019).
- [17] Y. Lia, Q. Gua, C. Chend, J. Zhangd, Q. Liud, X. Hua, J. Liug, Y. Liua, L. Lingg, M. Tiang, Y. Wangh, N. Samarthc, S. Lid, T. Zhangd, J. Feng, and J. Wanga, PNAS 115, 9503 (2018).
- [18] P. Hosur, X. Dai, Z. Fang, and X.-L. Qi, Phys. Rev. B 90, 045130 (2014).
- [19] M. Mandal, S. Marik, K. P. Sajilesh, Arushi, D. Singh, J. Chakraborty, N. Ganguli, and R. P. Singh, Phys. Rev. Mater. 2, 094201 (2018).
- [20] S. Kamboj, P. S. Rana, A. Sirohi, A. Vasdev, M. Mandal, S. Marik, R. P. Singh, T. Das, and G. Sheet, Phys. Rev. B 100, 115105 (2019).
- [21] A. Vasdev, S. Kamboj1, A. Sirohi, M. Mandal, S. Marik, R. P. Singh, and G. Sheet, J. Phys.: Condens. Matter 33, 255401 (2021).
- [22] R. P. Singh, A. D. Hillier, B. Mazidian, J. Quintanilla, J. F. Annett, D. M. Paul, G. Balakrishnan, and M. R. Lees, Phys. Rev. Lett. 112, 107002 (2014).
- [23] D. Singh, J. A. T. Barker, A. Thamizhavel, D. M. Paul, A. D. Hillier, and R. P. Singh, Phys. Rev. B 96, 180501

- (2017).
- [24] D. Singh, K. P. Sajilesh, J. A. T. Barker, D. M. Paul, A. D. Hillier, and R. P. Singh, *Phys. Rev. B* 97, 100505 (2018).
- [25] D. Singh, Sajilesh K. P., J. A. T. Barker, D. McK. Paul, A. D. Hillier, and R. P. Singh, *Phys. Rev. B* 97, 100505(R) (2018).
- [26] P. K. Biswas, H. Luetkens, T. Neupert, T. Sturzer, C. Baines, G. Pascua, A. P. Schnyder, M. H. Fischer, J. Goryo, M. R. Lees, H. Maeter, F. Bruckner, H. H. Klauss, M. Nicklas, P. J. Baker, A. D. Hillier, M. Sigrist, A. Amato, and D. Johrendt, *Phys. Rev. B* 87, 180503(R) (2013).
- [27] D. Singh, M. S. Scheurer, A. D. Hillier, D. T. Adroja, and R. P. Singh, *Phys. Rev. B* 102, 134511 (2020).
- [28] Arushi, D. Singh, A. D. Hillier, M. S. Scheurer, and R. P. Singh, *Phys. Rev. B* 103, 174502 (2021).
- [29] Y. Tanaka, Y. Mizuno, T. Yokoyama, K. Yada, and M. Sato, *Phys. Rev. Lett.* 105, 097002 (2010).
- [30] X. L. Qi and S. C. Zhang, *Rev. Mod. Phys.* 83, 1057 (2011)
- [31] J.-Q. Yan, B. C. Sales, M. A. Susner, and M. A. McGuire, *Phys. Rev. Mater.* 1, 023402 (2017).
- [32] M. Tinkham, ed., *Introduction to Superconductivity*, 2nd ed. (McGraw - Hill, New York, 1996).
- [33] E. Helfand and N. R. Werthamer, *Phys. Rev.* 147, 288 (1966).
- [34] N. R. Werthamer, E. Helfand, and P. C. Hohenberg, *Phys. Rev.* 147, 295 (1966).
- [35] K. Maki, *Phys. Rev.* 148, 362 (1966).
- [36] Y. J. Sato, F. Honda, Y. Shimizu, A. Nakamura, Y. Homma, A. Maurya, D. Li, T. Koizumi, and D. Aoki, *Phys. Rev. B* 102, 174503 (2020).
- [37] R. C. Morris, R. V. Coleman, and R. Bhandari, *Phys. Rev. B* 5, 895 (1972).
- [38] S. Yasuzuka, S. Uji, S. Sugiura, T. Terashima, Y. Nogami, K. Ichimura, S. Tanda, *J. Supercond. Nov. Magn.* 33, 953 (2020).
- [39] H. Matsuoka, M. Nakano, T. Shitaokoshi, T. Ouchi, Y. Wang, Y. Kashiwabara, S. Yoshida, K. Ishizaka, M. Kawasaki, Y. Kohama, T. Nojima, and Y. Iwasa, *Phys. rev. res.* 2, 012064(R) (2020).
- [40] Y. J. Hu, Y. Tai Chan, Kwing To Lai, K. O. Ho, X. Guo, H.-P. Sun, K. Y. Yip, Dickon H. L. Ng, H.-Z. Lu, and Swee K. Goh, *Phys. Rev. Mater.* 3, 034201 (2019).
- [41] Y. Tai Chan, P. L. Alireza, K. Y. Yip, Q. Niu, K. T. Lai, and Swee K. Goh, *Phys. Rev. B* 96, 180504(R) (2017).
- [42] J. M. Lu, O. Zheliuk, I. Leemakers, N. F. Q. Yuan, U. Zeltler, K. T. Law, J. T. Ye, *Science*, 350, 1353 (2015).
- [43] W. L. McMillan, *Phys. Rev.* 167, 331 (1968).
- [44] T. Klimczuk, F. Ronning, V. Sidorov, R. J. Cava, and J. D. Thompson, *Phys. Rev. Lett.* 99, 257004 (2007).
- [45] S. K. P., D. Singh, P. K. Biswas, A. D. Hillier, and R. P. Singh, *Phys. Rev. B* 98, 214505 (2018).
- [46] C. L. Zhang, S. Y. Xu, I. Belopolski, Z. Yuan, Z. Lin, B. Tong, G. Bian, N. Alidoust, C. C. Lee, S. M. Huang, T. R. Chang, G. Chang, C. H. Hsu, H. T. Jeng, M. Neupane, D. S. Sanchez, H. Zheng, J. Wang, H. Lin, C. Zhang, H. Z. Lu, S. Q. Shen, T. Neupert, M. Z. Hasan, and S. Jia, *Nat. Commun.* 7, 10735 (2016).
- [47] Y. Y. Lv, X. Li, B. B. Zhang, W. Y. Deng, S. H. Yao, Y. B. Chen, J. Zhou, S. T. Zhang, M. H. Lu, L. Zhang, M. Tian, L. Sheng, and Y. F. Chen, *Phys. Rev. Lett.* 118, 096603 (2017).
- [48] A. A. Burkov, *Phys. Rev. B* 96, 041110 (2017).
- [49] S. Nandy, G. Sharma, A. Taraphder, and S. Tewari, *Phys. Rev. Lett.* 119, 176804 (2017).
- [50] Y. Sun, S. C. Wu, M. N. Ali, C. Felser, and B. Yan, *Phys. Rev. B* 92, 161107 (2015).
- [51] Z. Wang, D. Gresch, A. A. Soluyanov, W. Xie, S. Kushwaha, X. Dai, M. Troyer, R. J. Cava, and B. A. Bernevig, *Phys. Rev. Lett.* 117, 056805 (2016).
- [52] X. Luo, F. Chen, J. Zhang, Q. Pei, G. Lin, W. Lu, Y. Han, C. Xi, W. Song, and Y. Sun, *Appl. Phys. Lett.* 109, 102601 (2016).
- [53] F. C. Chen, X. Luo, J. Yan, Y. Sun, H. Y. Lv, W. J. Lu, C. Y. Xi, P. Tong, Z. G. Sheng, X. B. Zhu, W. H. Song, and Y. P. Sun, *Phys. Rev. B* 98, 041114(R) (2018).
- [54] A. Soluyanov, D. Gresch, Z. Wang, Q.-S. Wu, M. Troyer, X. Dai, and B. Bernevig, *Nature* 527, 495 (2015).
- [55] P. Li, C. Zhang, Y. Wen, L. Cheng, G. Nichols, David G. Cory, G.-X. Miao, and Xi-Xiang Zhang, *Phys. Rev. B* 100, 205128 (2019).
- [56] P. Li, C. H. Zhang, J. W. Zhang, Y. Wen, and X. X. Zhang, *Phys. Rev. B* 98, 121108 (2018).
- [57] H. Li, H. Wang, H. He, J. Wang, and S. Q. Shen, *Phys. Rev. B* 97, 201110 (2018).
- [58] M. Wu, G. Zheng, W. Chu, W. Gao, H. Zhang, J. Lu, Y. Han, J. Yang, H. Du, W. Ning, Y. Zhang, and M. Tian, *Phys. Rev. B* 98, 161110 (2018).
- [59] Y. Sun, S. C. Wu, M. N. Ali, C. Felser, and B. Yan, *Phys. Rev. B* 92, 161107 (2015).
- [60] Z. Wang, D. Gresch, A. A. Soluyanov, W. Xie, S. Kushwaha, X. Dai, M. Troyer, R. J. Cava, and B. A. Bernevig, *Phys. Rev. Lett.* 117, 056805 (2016).
- [61] K. Zhang, C. Bao, Q. Gu, X. Ren, H. Zhang, K. Deng, Y. Wu, Y. Li, J. Feng, and S. Zhou, *Nat. Commun.* 7, 13552 (2016).
- [62] Y. Y. Lv, L. Cao, X. Li, B. B. Zhang, K. Wang, B. Pang, L. Ma, D. Lin, S. H. Yao, J. Zhou, and Y. B. Chen, *Sci. Rep.* 7, 44587 (2017).
- [63] S. M. Oliver, R. Beams, S. Krylyuk, I. Kalish, A. K. Singh, A. Bruma, F. Tavazza, J. Joshi, I. R. Stone, S. J. Stranick, and A. V. Davydov, *2D Mater.* 4, 045008 (2017).
- [64] X. J. Yan, Y. Y. Lv, L. Li, X. Li, S. H. Yao, Y. B. Chen, X. P. Liu, H. Lu, M. H. Lu, and Y. F. Chen, *npj Quantum Mater.* 2, 31 (2017).